THESIS FOR THE DEGREE OF LICENTIATE OF ENGINEERING

The Effects of Morphology and Surface Oxidation of Stainless Steel Powder in Laser Based-Powder Bed Fusion

DMITRI RIABOV

Department of Industrial and Materials Science

CHALMERS UNIVERSITY OF TECHNOLOGY

Gothenburg, Sweden 2020

The effects of morphology and surface oxidation of stainless steel powder in laser based-powder bed fusion
DMITRI RIABOV

Technical report no IMS-2020-4

Department of Industrial and Materials Science
Chalmers University of Technology
SE-412 96 Gothenburg
Sweden
Telephone + 46 (0)31-772 1000

Chalmers digitaltryck
Gothenburg, Sweden 2020

The Effects of Morphology and Surface Oxidation of Stainless Steel Powder in Laser Based-Powder Bed Fusion

DMITRI RIABOV

Department of Industrial and Materials Science
Chalmers University of Technology

Abstract

Laser based-powder bed fusion (LB-PBF) is one of the many techniques within additive manufacturing (AM) that allows for near net shape manufacturing of metallic components. By using powder feedstock, it is possible to spread thin layers of powder and further selectively fuse powder in a repetitive manner until the component is completed. The majority of the powder grades for AM are produced using vacuum induction melting and inert gas atomization (VIGA). The process produces spherical powder with high purity, but at a premium cost. In order to improve the utilization of LB-PBF further, more cost-efficient powder grades must be introduced to the market.

This work therefore addresses three grades of 316L stainless steel powder with regard to the surface oxide characteristics and processability in AM, a vacuum induction melted and inert gas atomized (VIGA) grade, an air-melted and nitrogen gas atomized (GA) grade and a water-atomized (WA) grade. The chemical surface characterization revealed that the two gas-atomized powders had comparable oxidation states, with minor differences in particulate coverage between the two grades. Since the GA powder contained more Si, it was found in higher concentrations in the oxide particulates. The WA grade, however, had a larger surface coverage of particulates (rich in Cr and Si), yet had a thinner oxide layer surrounding the particulates compared to the gas atomized grades. However, the particulate features on the WA grade did not seem to affect the printability, as densities of > 99.95% were reached without discernible defects in the microstructure. While the printability was comparable with the GA grade at a layer thickness of 20 µm, the limitation of the WA powder were noticed at a higher layer thicknesses (40 µm), where up to about 1 vol.% of porosity was obtained.

Furthermore, LB-PBF processing of WA powder was found to result in a rather homogenous precipitation of nanometric oxide inclusions within the microstructure. Consequently, this work investigated whether the oxide inclusions could contribute to an oxide dispersion strengthening effect. The average size of these oxides was found to be 56 nm, with an average number density of 2.8×10^{15} m^{-3}. The oxides were observed to be amorphous with a characteristic core-shell structure. Concerning the mechanical strength, the WA samples had slightly reduced yield strength (~500 MPa) in comparison to the GA samples (~600 MPa). Hence, no oxide dispersion strengthening effect was observed, as the average size and number density of oxides was not optimized.

Keywords: additive manufacturing, laser based-powder bed fusion, powder production, powder properties, powder surface, oxidation, morphology, 316L stainless steel, oxides

Preface

The work presented in this licentiate thesis was conducted at the Department of Industrial and Materials Science and the Department of Customization Technologies in Höganäs between May 2017 and June 2019. The work was conducted in the framework of the Center for Additive Manufacturing – Metal (CAM^2), supported by Vinnova, and was financially supported by Höganäs AB. The research was been conducted under the supervision of Professor Eduard Hryha and Professor Lars Nyborg at Chalmers and Adjunct Professor Sven Bengtsson at Höganäs AB.

List of appended papers

I. **Effect of atomization on surface oxide composition in 316L stainless steel powders for additive manufacturing**
D. Riabov, E. Hryha, M. Rashidi, S. Bengtsson, L. Nyborg
Submitted for journal publication

II. **Factors affecting printability of 316L powders using the DMLS process**
D. Riabov, S. Bengtsson
Proceedings of WorldPM2018 World Congress on Powder Metallurgy, 2018

III. **Effect of the powder feedstock on the oxide dispersion strengthening of 316L stainless steel produced by laser powder bed fusion**
D. Riabov, M. Rashidi, E. Hryha, S. Bengtsson
Submitted for journal publication

Contribution to the appended papers

I. The author planned and executed the majority of the experimental work and the analysis of the results. The author wrote the paper in collaboration with the co-authors.

II. The author planned and executed the experimental work and wrote the paper in collaboration with the co-authors.

III. The author was involved in the planning and execution of the experimental work together with the co-authors. The author analyzed the results and wrote the paper in collaboration with the co-authors.

Table of contents

1. Introduction

Since its industrial implementation, additive manufacturing (AM) has found several niche fields that have greatly benefitted from the design freedom, short lead times, high material utilization and part integration that the technology has allowed. Among these niche markets are medical, aerospace and the energy sectors – all of which require parts with high geometrical complexity, high material performance and low-volume production and limited cost sensitivity.

Within the umbrella term of AM, various techniques are used to build parts layer by layer. The powder bed fusion techniques utilize a high-power electron beam or laser (EB-PBF or LB-PBF, respectively) to selectively melt small amounts of powder, which is raked repeatedly over a build platform. The performance of the built part depends on the laser parameters and, to a great extent, the powder quality. Bad parameters can always be tweaked, but the quality of the powder cannot be changed without sending it back to the supplier.

A bottleneck for a wider commercialization of metal AM is the overall high cost of the process. Building a single part can take several days, and the material cost is substantial, with a price several times higher compared to a cast or forged part of the same alloy [1]. The high powder cost comes from the early days of metal AM, when the powder had to be manufactured using vacuum technology and argon atomization, setting the premium price. For example, dental crowns required cobalt-chrome alloys, which needed vacuum melting and argon atomization for chromium retention. Similarly, the aerospace industry required high purity Ni-based superalloys to maintain the performance and reliability of the parts they were producing. That set a precedent for the powder manufacturing process for metal AM.

One way to reduce the cost and expand the utilization of AM is to consider using powder produced by atomization methods commonly employed in other powder metallurgical fields, such as the metal injection molding industry (MIM). In the case of MIM, both air-melted (and atomized using N_2) powder and water-atomized (WA) powder are commonly used – in addition to the premium grades. Air melting can be suitable for alloys without large amounts of reactive elements (e.g., Al, Ti) and can achieve a similar quality to a vacuum melted powder. However, as nitrogen gas is not fully inert, it is possible that during atomization, the highly reactive powder surfaces can react with the gas. Thus, the formation of nitrides or carbonitrides is possible. Water atomization can accommodate similar elements to air melting, although reactive elements are generally avoided, and is capable of large-scale production. Due to the inertia of the water jet, together with the rapid cooling, the atomized powder has a very irregular shape. Additionally, since the WA grades are in direct contact with water during atomization, it leads to unwanted oxidation of the powder surfaces.

While the detrimental effect of oxides and oxide films on components produced by casting and other powder metallurgical processes are well understood, these effects are less known in the case of the aforementioned AM processes. In order to increase the use of more readily available and cost-effective powder within the field of AM, it is highly relevant to investigate whether and how the powder surface oxidation changes as the atomizing method is varied and how such changes affect the AM process robustness and the performance of AM-built parts.

1.1 Research objectives

The objectives of this work are to understand how different atomization processes affect the powder and its surface oxide state and how these influence the defect generation during LB-PBF processing. These objectives can be summarized in the following research questions:

- How does the atomization process affect the powder surface oxide characteristics?
- How does the powder surface oxide chemistry affect the LB-PBF process robustness, defect formation and the resulting mechanical properties of the built parts?
- What are the critical powder properties defining printing performance when using irregularly shaped powder in the LB-PBF process?

2. Powder based additive manufacturing

Contrary to, for example, metal cutting, which is a subtractive technology, AM builds up a geometry by successively adding material. The process of adding material can be achieved in numerous of ways and, for the sake of simplicity, can be compared to pottery or playing with Legos. Thus, material is only added where it is needed. However, as with pottery and Legos, the individual building blocks remain individual unless they are somehow fused. Pottery is burned to achieve this, and the Lego pieces can be glued together to achieve a similar cohesive structure. Essentially, AM is a combination of two steps: a means of assembling materials to form a required shape and fusing the material in order to hold the intended shape permanently. As one can imagine, there are numerous methods of achieving both, and a combination of these comprise the various AM processes. ISO 17296-2:2016 defines seven main groups [2]:

- Vat photo-polymerization
- Material jetting
- Binder jetting*
- Directed energy deposition*
- Material extrusion*
- Powder bed fusion*
- Sheet lamination

The focus of this work is on powder bed fusion, and more specifically on laser-based powder bed fusion. The other powder-based technologies AM (marked with an asterisk) are briefly introduced. A summary of the processes and characteristics of the utilized powder is provided in Table 1.

Table 1. Summary of powder-based AM technologies with some of their properties.

Process	Energy source	Particle size fraction (µm)	Available materials	Layer thickness (µm)
LB-PBF	Laser	10–60	13–18 [3]	20–60
EB-PBF	Electron beam	40–100	4 [4]	50–100
DED	Laser	50–150	17 [5]	> 1000
Binder jetting	Furnace heating	< 20	5–6 [6], [7]	20–50
Extrusion	Furnace heating	< 20	4 [8]	100–200

AM has recently seen an upswing in media, the scientific community and commercialization. An article from *The New York Times* [9] from 2010 calls 3D printing a “manufacturing revolution.” While a revolution has not yet occurred, the technology has found some niche fields in which it is able to compete with traditional manufacturing processes. Siemens Industrial Turbomachinery AB, a company specializing in gas turbines for energy generation, adopted AM to produce and refurbish burner nozzles found in their gas turbines. By doing this, they reduced 13 parts down to 1, while also eliminating the need for 18 welding operations. The dental and orthopedic industries can customize implants through AM, improving the osteointegration and performance of the implants [10]. In a recent report [11], the field is expected to grow by 27% annually, providing a positive outlook for the future.

The tooling industry could draw benefits from the technology, reducing lead times and increasing the capacity. However, this field has not yet had the same impact as the cases mentioned earlier. The scarcity of available materials for tooling applications and high costs are identified as the biggest challenges [12]. Therefore, exploring new low-cost materials and adding materials that are commonly used in these fields is important for the further development of AM.

2.1 Powder bed fusion

Powder bed fusion (PBF) systems are defined according to their principle, where a powdered material is fused layer by layer using an energy source. The energy source is either a laser (LB-PBF), or an electron beam (EB-PBF). The general working principle is similar between the two, with methods of beam deflection and the process gas environment (vacuum or inert gas flow) being the greatest differences. In LB-PBF, deflection is done through galvanometers, compared to the magnetic lenses of EB-PBF. The major components of a PBF system can be seen in Figure 1. Generally, the build cycle starts by applying an initial thin layer of powder onto a build plate. The system is then either pumped to a low vacuum in the case of EB-PBF or flushed continuously with an inert gas in the case of LB-PBF. This is done to minimize the oxidation during the laser exposures.

In LB-PBF, when a pre-set oxygen level within the system is reached, the selective exposure of the first layer is carried out. After the exposure, the building platform is lowered to be equal to the set layer thickness. Similarly, the dispenser platform is raised, the height of which depends on an algorithm that considers the exposed area, the layer thickness and other factors to ensure that required amount of powder for full coverage of the build plate has been added. The re-coater then rakes the powder over from the dispenser to the building platform. Any surplus of the powder, or debris from the previous exposure, would be raked into the powder collector. The steps of exposing, lowering the platform and raking the powder are repeated until the part is complete.

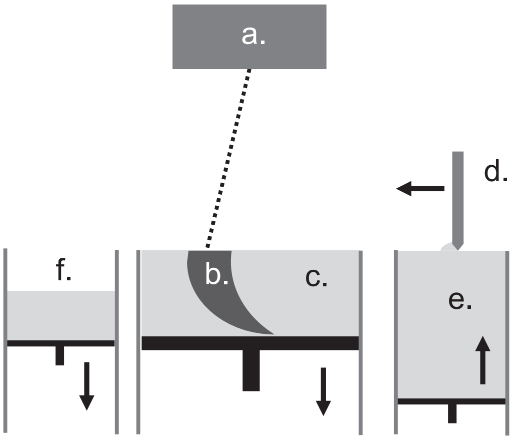

a. Laser and galvanometers
b. Part
c. Powder and building platform
d. Re-coater
e. Powder dispenser
f. Powder collector

Figure 1. Schematic of a simplified LB-PBF system. The arrows indicate the relative movement of the platforms.

After completion, the powder is recovered through a vacuum system and sieved to remove spatter and debris from the build before being re-used. The building platform is then removed from the machine and post-processed. Post-processing steps can include the removal of supports, heat-treatment and machining.

The required powder properties for the beam-based PBF processes vary between the two beam types. LB-PBF requires powder with high spreadability and high powder-packing densities, and highly spherical powder is thus commonly used. However, they must be fine enough to be able to print with thin layers, which produces good surfaces and allows for fine features in the printed component. The typical size ranges are between 10 and 60 µm. The powder for EB-PBF is often somewhat coarser, between 40 and 100 µm, as finer powder increases the tendency of a phenomenon called smoking. Smoking occurs when the powder particles are charged by the electron beam rather than melted, causing them to disperse and form a smoke-like cloud; see Figure 2. Smoking can also be caused by electrically insulating oxide layers on the powder, preventing them from conducting the electron beam. Therefore, some cleanliness requirements for powder in EB-PBF can be of practical significance [13].

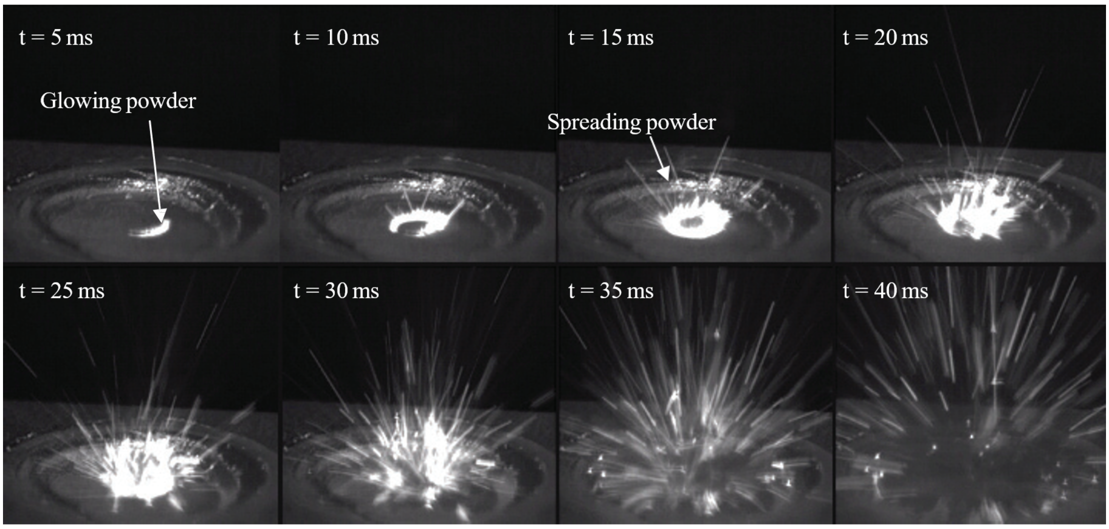

Figure 2. A sequence leading up to a smoke-event in EB-PBF. Reproduced with permission from Springer Nature [14].

2.2 Directed energy deposition

Like the powder bed systems, directed energy deposition (DED) involves a laser source that melts powder particles as they are deposited. However, both the laser focusing system and the powder delivery systems are integrated into a single nozzle or deposition head; see Figure 3. The deposition head can then be co-axially placed onto a robotic arm, and the part is subsequently built on a stationary or moving worktable. The laser source is usually a fiber laser operating at powers between 0.5 and 3 kW, and thus, the energy is higher than in LB-PBF systems, allowing for faster build rates. The typical spot size is around 1 mm in diameter, and hence, fewer finer details can be achieved. Since there is no build chamber, the build volume is only limited by the reach of the robotic arm, and build volumes can thus be up to one cubic meter [15]. The powder is blown directly into the melt pool and fed through tubes with the help of a pressurized inert gas. By having several powder feeding mechanisms, blends of powder can be used, making it possible to create graded materials.

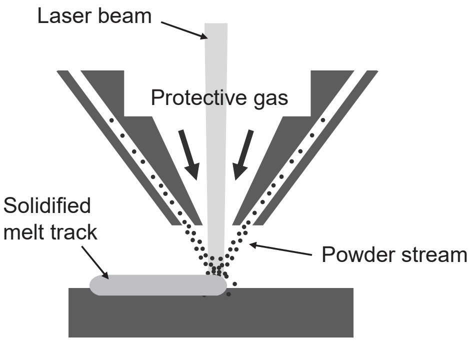

Figure 3. Schematic of a coaxial DED nozzle.

The powder used in this process is typically gas atomized and melted in either air or a vacuum, depending on the alloy. Size distributions are commonly between 50 and 150 µm, however, finer fractions are also used when better surfaces are required. There are high demands on high powder flowability, as the tubes feeding the powder to the nozzle can easily clog. The powder therefore must have a minimal amount of both satellites and fines (particles < 10 µm).

2.3 Binder jetting

Binder jetting technology is very similar to the PBF technologies, as the process involves similar parts. However, no actual fusing or melting takes place. The electron beam or laser is replaced with an inkjet-like printer head. As the head traverses the powder bed, it dispenses very small amounts of a liquid binder that binds the powder particles together. The printed geometries must be sintered to attain their full strength, where the sintering process and the component properties are similar to conventional powder metallurgy, specifically MIM. The sintering process allows the individual particles to fuse together under high temperatures. The binder jetting process has significantly higher build rates compared to the other powder bed systems, but the process is limited to smaller part sizes.

The required powder for binder jetting must be high flowing to ensure proper spreading across the powder bed. Additionally, as the process involves sintering, which is thermodynamically driven by the reduction of the surface area, the powder particles must be small, typically below 20 µm. However, powder below 20 µm generally do not flow well, and any satellite features therefore impede it even further; hence, satellite free powder is essential. Generally, minor surface oxidation of such powder tends to not be a problem, as high temperature sintering in a vacuum or reducing atmospheres reduces them, unless the oxides are very stable (e.g., Al_2O_3, MgO, etc.). Such oxides tend to either reduce the mechanical performance of the built part or hinder the densification process during sintering, rendering porous parts.

2.4 Material extrusion

Material extrusion had the biggest breakthrough with the consumer-based printers, which brought the ability to print polymer materials at home. A thermoplastic filament is heated to its melting temperature and extruded layer by layer onto a build plate. By admixing metallic powder into the polymer and extruding it into a filament, metallic components can also be printed using this technology. However, similar to binder jetting, the parts must subsequently be sintered. Additionally, prior to the sintering stage, the thermoplastic must be removed, since this affects the sintering cycle. While this step also exists in binder jetting, the amount of added polymer in the filament is considerably larger, and thus, the attained final density is quite low in comparison.

The powder requirements in material extrusion are similar in some aspects to binder jetting, as they must be able to sinter well. However, since the powder is admixed into a moldable filament, the powder flow characteristics become less important. The benefit can be that powder aimed for MIM can be used, since the process is quite similar.

2.5 Considerations specific for LB-PBF

Scanning strategy and parameters

The scanning strategy of an LB-PBF system is unique to the machine supplier, and often, a part of their intellectual property since the parameters and strategies define many of the important properties of the built part. Process parameters define to a large extent the part density, microstructure, defect state, surface roughness and residual stresses. The strategy defines how the laser scans over the part, including how the outer perimeter (contour) is exposed before the bulk or vice versa. The parameters define at which speed the laser (in mm/s) is scanned, with which laser power (in W) and the gap between each scan vector (hatch distance, in mm) and so on. Most machine suppliers have developed optimized strategies and parameters for various materials, to which the customer gains access.

The speed at which a part can be built depends on multiple factors, namely, the scanning speed, the hatch distance and the layer thickness, and the product of these three factors is the build rate. While the build rate can be tuned to run at the maximum capacity of the galvanometers, this is generally avoided, since the part quality will rapidly deteriorate. Similarly, too large layer thicknesses require very high laser powers and decreases the surface quality of the built part.

As mentioned, gains in build rates generally come at a cost of part quality and vice versa. While the build rate can easily be calculated, estimating the build quality is generally more difficult. A commonly used equation to estimate the parameter range for good quality is the volume energy density (VED) expressed as follows:

$$VED = \frac{P}{V\,H\,L} \tag{1}$$

where P is the laser power, V the laser scanning speed, H the hatch distance and L the layer thickness. This equation indicates whether a parameter combination has a theoretically sufficient energy density to produce a dense part. However, the VED is a very crude estimation, considering that it does not take into account melt pool dynamics, the laser intensity or any material properties. A heat flow model proposed by Thomas et al. [16] and further elaborated by Ion et al. [17] is a more refined method to predict the quality since it considers the material properties to create processing maps using normalized parameters. Thus, it is possible to theoretically correlate build rates to the resulting predictions of part quality.

There are many other indirect parameters to the LB-PBF process, as compared to the more direct parameters mentioned above. Some of the indirect parameters include build plate pre-heating temperature, re-coater traverse speeds, turbine power (regulating the gas flow over the build chamber) and powder feed.

Influence of the powder properties

The powder bed systems rely heavily on the ability of the powder to spread, which is often described as the ability of powder to flow. To be more precise, the rheology of the powder is very important to ensure that the powder possesses the necessary level of spreadability.

The powder rheology is dependent on many characteristics of the powder, such as the morphology, cohesivity, electrostatic charging and particle size distribution. It also depends on external parameters such as humidity and temperature. Flow has traditionally been defined as the time it takes for 50 g of powder to flow through a Hall-flow funnel (a standardized 60° cone with a 2.5 mm orifice at the bottom). While this flow test was made to be easily accessed and replicated, it is more suitable to define the powder rheology relevant for the press and sinter routes rather than AM. Hence, its relevance to the powder bed systems has been questioned [18]–[20] due to the limited ability of the Hall-flow funnel to measure powder that is cohesive, since these generally do not flow through a Hall-flow funnel. However, such powder can still work well in powder bed fusion systems, for example, powder for binder jetting.

Therefore, alternative methods of measuring powder rheology are being investigated. One of the studied methods is based on the utilization of a powder rheometer – capable of measuring bulk, shear and static properties with high precision. While some groups have reported on the ability to distinguish between virgin and recycled powder [21], the industry has not fully adopted the method due to the large scatter and heavy operator dependence of the system. Another method that has seen wide application in the AM community is the revolving drum analyzer. In this method, the avalanche angle of powder is continuously analyzed through imaging as the drum rotates. Spierings et al. [19] found the method to quantitatively distinguish between well-flowing powder and powder that did not flow.

Generally, a disconnect between measured powder properties and powder performance within the LB-PBF process remains due to the complexity of powder spreadability [22]. Karapatis [23] showed that in experimental raking trials, powder flow and the packing density of the powder were the main properties governing the raked powder layer density. The same study also showed that increasing the layer thickness also increases the powder layer density. Strondl et al. [18], in connecting powder properties to build quality, showed that certain variations in the powder feedstock do not affect raking or melting significantly.

Laser–powder interactions

Traditionally, laser welding operates under a welding mode called key-hole welding. The welding mode ensures deep penetration of the laser, assuring good fusion between weldments. Another welding mode is conductive welding, in which the key-hole is suppressed. The key-hole forms as the melt begins boiling and evaporating, with the evaporation creating a vapor pressure normal to the melt surface that, together with the Marangoni flow, pushes melt away from the point of irradiation [24], [25]. The Marangoni flow is a hydrodynamic motion caused by the change in the viscosity of the liquid metal as the temperature changes [26]. Thus, colder sections of the melt *pull* the hotter melt towards it, as the cold sections are more viscous (under the condition that viscosity decreases with temperature). Typically, this creates a strong swirling and mixing effect (see Figure 4), which is further enhanced in the presence of strong thermal gradients. The melt flows from the point of irradiation to the solid interface at the border, but this depends on how the viscosity changes with temperature [26].

The way the laser interacts with the powder bed to melt and form continuous melt tracks is very similar to conventional laser melting. The initial interaction when the melt pool is formed is, however, different. Contrary to a dense metallic surface, a powder bed allows for multiple reflections of the laser. This allows for a higher absorptivity of the laser, reaching values of 0.6–0.7, compared to the 0.4 of a bulk stainless steel surface [27], [28]. Due to the high scan speeds (up to 7 m/s) in LB-PBF, the laser irradiation of individual powder particles is very rapid, somewhere between 0.2 and 8 ms. Thus, the melting process starts with a concentration of the thermal energy at the skin of the powder particle, which takes up to 80 ms to dissipate to the rest of the powder particle when the entire particle melts [29]. As several molten particles coalesce, the melt pool is formed.

From studies utilizing high-speed imaging to observe LB-PBF melt pools [27], it can be postulated that the powder particles are engulfed in the melt-pool ahead of the laser as it traverses. Thus, the laser irradiates mostly the liquid melt pool, which in turn induces a shallow key-hole like depression, as described earlier. Hence, the LB-PBF process operates somewhere between conduction and key-hole welding, and the magnitude of the vapor pressure is not as strong as in pure key-hole welding. The induced vapor flow from the key-hole creates a drop in pressure in its vicinity and creates a secondary inward flow of the cold processing gas [30]. These induced flows affect the powder particles adjacent to the melt pool, as seen in Figure 4, which shows that most of the observed spatter does not necessarily come from the melt pool itself [27], [31], [32]. Some of the spatter originates from the hydrodynamic forces of the melt pool, ejecting splashes from the primary melt pool [32].

Additionally, the in-situ work of Leung et al. [33] showed that powder adjacent to a melt track can be ejected, as the gas found in the voids of the powder bed superheats and rapidly expands, suggesting that optimal packing densities are favored, since less de-gassing of the powder bed need occur. However, studies involving non-optimal powder is limited, and as such, understanding of the interaction is lacking.

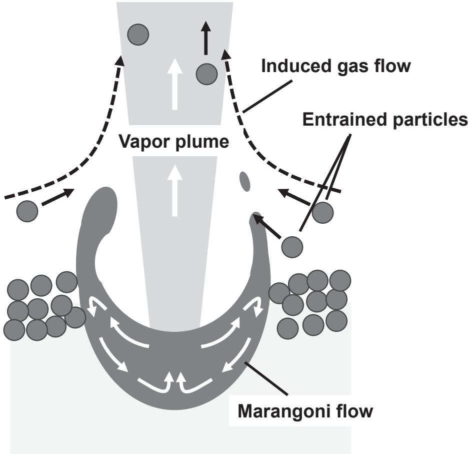

Figure 4. Schematic of the melt pool with generated vapor flow and secondary gas flow.

3. Powder manufacturing

Most of the powder used for LB-PBF is of premium grades, with tight specifications on impurities and with optimal flow characteristics. The drive for such powder originated from times at which AM was solely a small niche production method for dental implants and medical applications [34]. Materials for these applications required vacuum melting and high purity gases for the powder production, leading to a high material cost. In spite of this, the demand for AM parts was large enough that the cost of materials became marginable and, therefore, cost optimization of the powder grades was not prioritized. As more materials were introduced into the materials portfolio, the production methods remained the same. To ensure the further growth of AM, an expansion into applications that are more cost sensitive must be pursued. An important step in this expansion is the development of lower-cost powder for AM and the exploration of alternative powder manufacturing routes.

3.1 The melting process

While some metallic powder can be produced without prior melting of the material, such as the sponge iron, most of the metal powder produced today for the AM field requires prior melting. Conventional melting practices for powder pre-cursors can be separated into two sub-groups, one in which the melting is done under a protective atmosphere or vacuum and one in which the melting occurs in a furnace exposed to air. Most of the conventional steel industry employs the latter, with the melt being exposed to air during processing. However, molten steel is highly reactive and rapidly oxidizes if it comes into contact with oxygen.

Therefore, the melt must be protected from the surrounding air. This can be done by adding a layer of liquid oxides to the surface of the molten metal. The layer, also called the slag layer, naturally remains buoyant on the surface due to its low density and acts as a diffusion barrier for oxygen. Furthermore, steelmakers have found ways to utilize the slag layer as a means of refining the steel. Through additions of quicklime and magnesite, it is possible to purify the melt from detrimental elements such as sulfur and phosphorous. Oxidized iron can be recovered from the slag by injecting carbon into the surface of the melt, which reduces oxidized iron into metallic iron. Alloying can also be adjusted easily on the fly, since the furnace is open, and access is easy to add necessary elements. The drawbacks, however, are that highly reactive materials (e.g., Ti, Al) are not able to be processed in this way. During melting and refining, the reactive elements are selectively oxidized and float up to the slag layer, where they remain. Nonetheless, open-air melting does not produce steel of worse quality; the process simply cannot accommodate reactive materials.

To be able to process alloys containing reactive metals, it is necessary to melt them in a vacuum. In vacuum melting, the whole system is pumped down to 10^{-3} mbar pressure to avoid unwanted oxidation of the melt [35], requiring extensive pumping infrastructure. Charging must thus be carefully calculated and prepared beforehand and cannot be adjusted on the fly. Melt de-oxidation occurs through an initial carbon boil [36], in which non-reactive elements are combined with a minor addition of carbon, which reduces a majority of the oxygen. Subsequently, the reactive elements are added, with the remainder of the oxygen removed through the vacuum/melt interface. Hence, slag systems are not utilized during vacuum melting.

3.2 Atomization

Atomization is the process of disintegrating a liquid metal stream into droplets by means of an accelerated medium. During cooling, the disintegrated droplets can either spheroidize or remain in an irregular shape, depending on the cooling capability of the atomizing medium. Among the gases, the most frequently employed are argon and nitrogen, and compressed air and helium are used too, though less commonly. While when using liquids, the dominant liquid is water; exotic liquids such as kerosene have also been used. The inert gases have the advantage of significantly limiting the oxidation of powder surfaces, and gas atomization thus becomes more suitable for atomizing reactive elements. The main drawback is due to the low density of gases, less energy is available to break apart the melt stream into droplets. The productivity can be increased when using water, since more energy is available for the disintegration. For a comparison, the properties of argon, nitrogen and water relevant for atomization can be found in Table 2.

Table 2. Physical and chemical properties of different atomizing media [37].

Atomizing medium	Density at 0 °C [g/cm^3]	Specific heat capacity at constant pressure [J/(kg K)]	Volumetric heat capacity [J/(m^3 K)]
Ar	0.0017	520	850
N_2	0.0013	1000	1200
H_2O	1.0	4200	$4.2\ 10^6$

The practical aspects of atomization are similar whether gas or water atomization is used, and a schematic of the process is provided in Figure 5. As the first step, the raw material is both melted and super-heated to decrease the viscosity of the liquid and to additionally compensate for the heat-loss as the melt is handled further. The liquid metal is then poured into a pre-heated tundish. The tundish has a circular orifice at its bottom, with a diameter optimized for the process and the wanted size distribution. The diameter of the orifice is an important parameter in atomization, as it controls both the productivity and the average powder particle size, since larger diameters allow for a greater flow of the melt. A stopper rod mechanically blocks the orifice until the melt is ready to be atomized. Located under the tundish orifice is an atomizing nozzle, which supplies the pressurized atomizing medium.

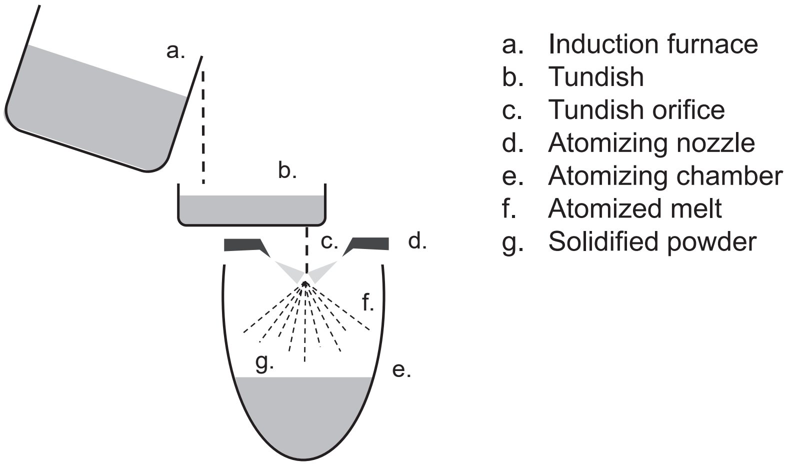

Figure 5. Simplified schematic of an atomizing facility. Re-drawn from [38]

Nozzles are often complex in design and can be arranged in various ways to provide different geometries at which the atomizing media contacts the melt stream; examples include V-jets and annular designs. V-jets in particular can be configured in multiple of ways (see Figure 6) and are most commonly used for water atomization, while annular designs are most common in gas atomization. The nozzle can be placed either directly under the orifice of the tundish or at a distance from the tundish, allowing the melt to free fall before being hit by the atomizing medium. The former configuration is called close-couple atomization and is more frequently employed in the production of fine gas atomized powder. The latter is called free-fall atomization, which is a more traditional arrangement for powder atomization.

When the stopper is lifted, the metal stream can flow into the atomizing jets, where it disintegrates, forming ligaments that rapidly decompose into droplets. In most cases, gravity is the only force acting on the melt as it flows through the orifice, but it is possible to apply an external pressure. The powder can then be collected at the bottom of the atomizing chamber and processed further, for example, dried, screened and sieved. While this is a general procedure for the atomization of metals, there are some aspects specific to gas atomization and water atomization, which are considered below.

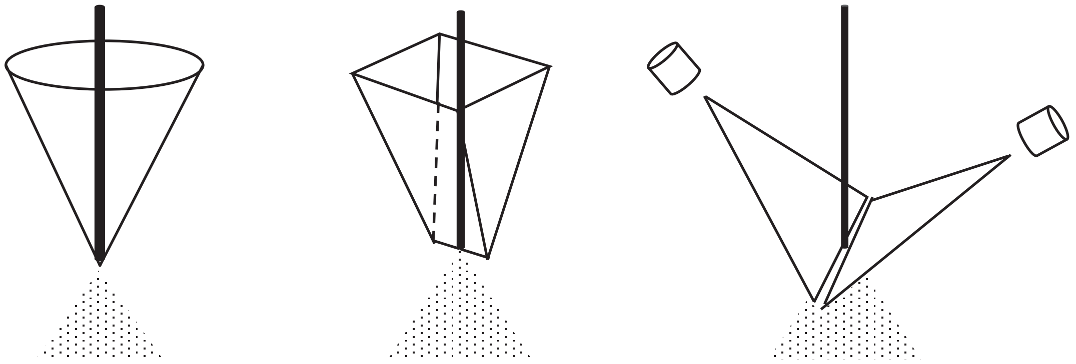

Figure 6. Different ways of arranging V-jets. Re-drawn from [38].

Inert gas atomization

Inert gas atomization, coupled with vacuum melting, can produce very clean powder even when melting reactive elements. However, the productivity is low, and the powder particle distribution is rather wide with an average particle size of 100 µm, causing low yields. Some findings report that the average yield for a typical LB-PBF sieve cut of 25–63 µm is around 15% [39]. The mean particle size can be reduced by using a close-coupled nozzle, making close-coupled nozzles more suitable for powder aimed to be used for AM. The size distribution can be tuned further through careful selection of the atomizing pressure and the nozzle design [40], [41]. Close-coupled nozzles are, however, more prone to process interruptions, as nozzle clogging occurs more often [38]. The clogging issue originates from the flow paths of the gas as it exits the annular nozzle, creating a cone with the perimeter comprising a high-velocity gas. Inside the cone, the pressure tends to drop, which pulls particles and droplets back into the orifice. This effect can be remedied through nozzle design, in which a portion of the atomizing gas is introduced into the cone – thus relieving some of the vacuum [38]. The turbulence can cause other detrimental effects, such as an increased tendency of satellite formation. Satellite formation occurs when smaller-sized particles weld to larger particles, as these take longer to form a solid outer skin [39]. Excessive satellite formation often affects the powder flow detrimentally, in some cases causing the powder to be rejected, as it no longer fulfills the specification; see Figure 7.

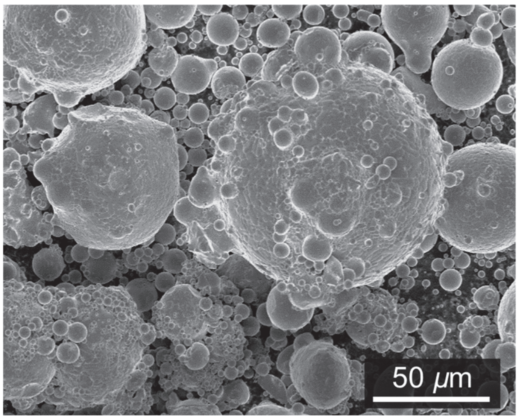

Figure 7. A gas atomized powder with excessive satellite formation.

The effect of atomizing gas on the resulting powder was extensively studied by Ünal [42], in which argon, nitrogen and helium were compared. Helium was found to produce powder with the smallest mean particle size, followed by nitrogen and lastly, argon. This was attributed to the ability of the specific gas to attain the highest gas velocity. Another aspect of inert gas atomization is the formation of internal gas porosity. While helium and argon are truly inert gases, they also have very limited solubility in most metals. Thus, if such gases were to be dissolved in a super-heated melt, upon cooling, they can re-precipitate as voids. Similarly, if entrapped during atomization, these voids remain. By contrast, nitrogen can dissolve in common engineering materials, which may remedy the problem of internal gas porosity [43]. Rabin et al. [44] reported on entrapped gases in atomized powder, in which it was concluded that most of the gas was trapped in macroscopic pores. It was also reported that the majority of the pores were in particles larger than 75 µm, and the most likely formation mechanism was during the liquid droplet formation (where a liquid ligament closes in on itself) [44], but not excluding gas dissolution from the melt.

Gas atomized powder is mostly spherical (see Figure 8), often with visible dendrites on the surfaces. The powder can efficiently pack to high packing densities, up to 60% of the full density, or 5 g/cm^3 (for steel powder), while also having high powder flowability.

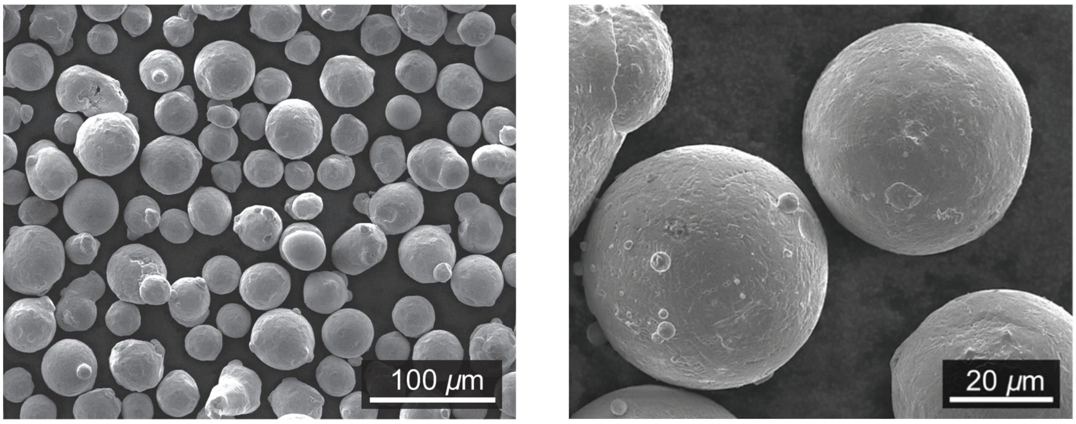

Figure 8. A typical gas atomized powder in the sieve fraction 20–53 μm.

Water atomization

Water atomization (WA), contrary to gas atomization, neither produces similar cleanliness of powder, nor is it possible to process reactive materials. It is, however, possible to produce large quantities of powder due to the large amount of energy in a pressurized water jet. Water pressures of 10–15 MPa are used to produce steel powder for the press and sinter routes, thus rendering a mean particle size of around 70 μm [45]. Finer powder can be achieved by using significantly higher water pressures, up to 150 MPa, which reduces the mean powder particle size to below 10 μm [46]. As in the case of gas atomization, the process is tunable and allows for a particle size optimization. Water also has a higher thermal capacity than gases, which causes a near instant solidification during atomization, which is why WA powder has highly irregular shapes; see Figure 9.

The oxidation of WA powder cannot be avoided, but there are ways of minimizing it. In a review by Dixon [38], one possible way is to increase the amount of water in the settling tank (the tank where the water is collected together with the powder) to keep it at a level near the nozzle. Thus, the powder is quenched more rapidly. Another way is to introduce inert gas into the atomizing chamber. This is common practice already to reduce the risk of hydrogen combustion when the water dissociates during atomization [45]. In some cases, the inert gas is already introduced in the atomizing nozzle, both to reduce oxidation and as a first step to disintegrate the melt. The process is called hybrid atomization, as both media act to disintegrate the melt stream [47].

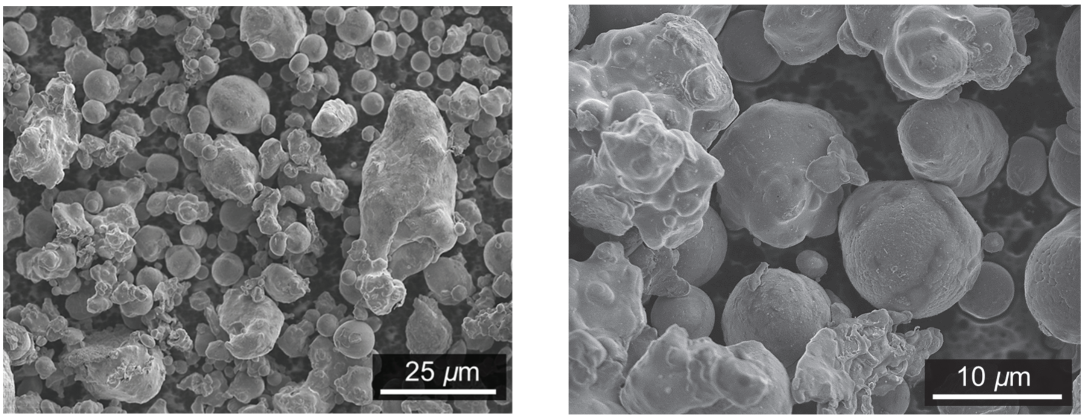

Figure 9. Micrographs of typical WA powder in an as-atomized state.

4. Oxides and the LB-PBF process

4.1 Thermodynamic considerations

This chapter aims to introduce some thermodynamic considerations to help understand the driving forces behind formation of oxides and their stability ranges.

The driving force behind all chemical reactions is the change in the Gibbs free energy ΔG. For a spontaneous reaction to occur, the Gibbs free energy of the system has to decrease relative to what it was before the reaction. Oxidation occurs only when ΔG is negative, which is often the case for oxide formation. For most metals, the oxide is more stable than the metal under normal conditions. For any reaction the free energy change can be expressed as $\Delta G^0 = \Delta G + RT \ln K$, where ΔG^0 is the standard free energy change and K is the equilibrium constant for the reaction. At equilibrium $\Delta G = 0$, the standard free energy change (ΔG^0) can be written as:

$$\Delta G^0 = -RTln(K) \tag{2}$$

For oxide and metal activities of unity the expression simplifies to:

$$\Delta G^0 = -RTln(p(O_2)) \tag{3}$$

The Ellingham diagram is a collection of standard free energy change values ΔG^0 as a function of temperature for the formation of many oxides, as shown in Figure 10. In general, metal oxides become less stable as the temperature increases, as indicated by the positive slope of the plots. The Ellingham diagram can also be used to obtain the partial pressure of O_2 required to form oxide at any temperature. While the Ellingham diagram predicts whether a reaction is likely to occur, it does not take into consideration the rates of reactions. Hence, kinetics influencing the formation and growth of oxides should be additionally considered.

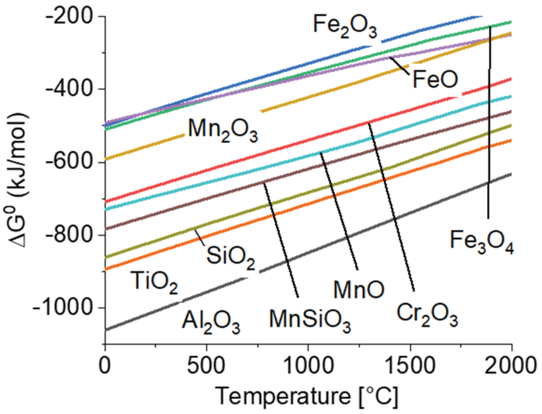

Figure 10. Ellingham diagram for selected oxides; data from HCS Chemistry.

The following reaction is behind the Ellingham diagram:

$$\frac{2x}{y}M + O_2 = \frac{2}{y}M_xO_y \tag{4}$$

The two other reactions by which an oxide can be reduced are the carbothermic reactions (direct and indirect) and the reduction by hydrogen gas. The carbothermic reactions are stipulated below:

$$\frac{2}{y}M_xO_y + 2C = \frac{2x}{y}M + 2CO \tag{5}$$

$$\frac{2}{y}M_xO_y + 2CO = \frac{2x}{y}M + 2CO_2 \tag{6}$$

Similarly, the reduction by hydrogen:

$$\frac{2}{y}M_xO_y + 2H_2 = \frac{2x}{y}M + 2H_2O \tag{7}$$

Thus, metal oxides can be reduced by dissociation, carbothermal reduction and reduction by hydrogen gas.

4.2 Surface oxide state of the powder

The oxide state of the powder has been a topic ever since pre-alloyed powder, containing stable oxide-forming elements, started being atomized and utilized to produce components. The oxides, if not reduced during processing such as sintering, would remain in the sintered components, reducing the mechanical strength of the final parts. Proper characterization of the powder surfaces provided an understanding of how the sintering cycle could be altered so that the oxides could be efficiently reduced. This section aims to introduce the surface oxide composition of the powder, ways to characterize the surface oxides and which oxidation products are commonly found on the water and gas atomized powders.

Olefjord and Nyborg [43] began adapting surface sensitive characterization techniques, such as X-ray photoelectron spectroscopy and Auger electron spectroscopy, to analyze metal powder and the surface oxidation of such in the early 1980s. The challenge of such techniques was the angular dependence of the generated electrons from a non-planar surface. Therefore, geometrical relationships had to be developed, allowing for an accurate data interpretation [48]. Early work on a nitrogen-atomized ferritic chromium steel powder [43] was able to provide details on the oxide speciation, the thickness of the oxide species and the coverage of certain oxide species relative to the total area of the powder surface. Chromium, manganese and silicon oxides in particulate form were depicted to cover > 70% of the surface. The area surrounding the particulates was a 3 nm layer of Fe_2O_3. It was further postulated that the particulate oxides formed during the atomization process, while the iron oxide grew during the subsequent cooling and handling of the powder, for example, its initial exposure to the ambient air.

The efforts were extended to investigate factors affecting the formation of surface oxides. The influence of the particle size was researched, where particles smaller than 40 μm tended to have thinner oxide layers, yet the oxidation of elements with high affinity to oxygen was more prominent [49], [50], whereas powder particles showed an average oxide thickness independent of particle size. In a study in which 12% Cr steel powder was fabricated using the rotating electrode process in argon with varying oxygen level, the oxidation of the alloying elements was found to differ according to the amount of residual O_2 in the gas [50]. Therefore, if the atomizing gas is very lean on O_2, elements with the highest oxygen affinity preferentially oxidize; while oxidation of, for example, the base metal will be more pronounced with increasing oxygen availability. Hence, the diffusivity and the availability of the elements plays an important role, and there is a competitive growth of oxides involving elements having varying oxygen affinity on a powder particle surface.

The adoption of surface sensitive techniques was extended to WA powder by Tunberg and Nyborg [51]. The WA powder grades, if in the size range of below 50 µm, had similar oxide layer thicknesses as the gas atomized grades. Thus, the surplus of oxygen in the WA grades is due to the larger specific surface area, rather than thicker oxidation products, when considering LB-PBF relevant powder sizes. Tunberg and Nyborg [52] showed in a study of WA 304L with additions of aluminum that Al was oxidized preferentially in the fine fractions of the powder, while the formation of other commonly found oxidation products was suppressed, showing the limitations of using water atomization to process reactive elements. It was also found [52] that the oxide composition and formation was highly dependent on the cooling rate and was found to be the rate limiting factor.

4.3 Oxide characteristics and their impact on the properties of LB-PBF components

In PM, processing routes such as press and sinter and MIM, most of surface oxides are reduced during sintering, and only their residues can be found in the interparticle boundaries, whereas in the case of hot isostatic pressing, oxides from the powder surfaces are carried over to prior particle boundaries [53], [54]. Thus, changes in both chemistry and morphology of oxides can be tracked relatively easy. However, due to the rapid nature of LB-PBF melting, the mechanism behind the oxide transfer into consolidated components is more difficult to establish. Understanding the processes happening with the surface oxide will provide insights into the relevance of the powder surface state and the oxygen content on the final build quality.

A better introspective into possible mechanisms can be made through the published work on inclusions in traditional weldments using laser or electron beam as the energy source. Babu et al. [55] developed a generalized inclusion model to predict the inclusion formation in low-alloy steel welds. The model assumes all deoxidizers and oxygen to be in solution as the starting point and assumes the first nucleation to be homogenous. The first oxide to nucleate is defined according to the magnitude of the driving force ΔG, while secondary oxides are nucleated heterogeneously on the primary oxides. The nucleation rate of the first oxide also depends on the assigned cooling curve. The model was further developed to include Marangoni flows and predicted coarsening of inclusions associated with their collision and coalescence [56]. The model was verified against experimental work and showed good coherence [57], providing a mechanistic explanation of nucleation and the growth of inclusions. The work of Matsumiya et al. [58] within the same topic employed a thermodynamic model rather than the kinetic model proposed by Babu. The modeling effort incorporated the use of finite element methods to calculate equilibriums and solute diffusion at the solid–liquid interface. This allowed inclusions to change composition and even dissolve as the solidification would progress, taking into consideration their stability range and composition of the liquid metal. However, the model was not created specifically for welding applications; rather, the intended use is for inclusion and segregation control in casting.

Recent efforts of Gruber et al. [59] showed that despite the high temperatures of EB-PBF, Al-rich surface oxides of IN718 powder were found to melt, contrary to being dissolved. Furthermore, the oxides were occasionally found to agglomerate and solidify into micrometer-sized defects. These larger defects were no longer able to melt and disperse; rather, they remained within the microstructure. Hence, despite the high temperature involved in the EB-PBF process, the oxides can remain in the liquid without dissolving, which shows that the models described above cannot always predict the inclusion characteristics accurately. Gruber et al. [59] also showed that the biggest contribution to these oxides comes from powder re-use rather than atomization. Hence, special care should be taken during the PBF processing of such alloys.

5. Experimental methods

In this study, three powder grades supplied by Höganäs AB, Sweden, of nominal 316L chemistry were analyzed. The aim was to investigate effects of different atomization techniques on the surface oxide chemistry and printability utilizing the LB-PBF process. The effect of higher oxygen contents on the final part properties was also studied. The following powder grades were examined:

- Vacuum inert gas atomized, using Ar – abbreviated VIGA
- Air melted and gas atomized, using N_2 – abbreviated GA
- Air melted and water atomized – abbreviated WA

The powders were characterized with respect to their physical properties (densities, particle size distribution etc.) using conventional PM methods and complemented with a powder rheometer. The chemical compositions were also measured and are provided in Table 3.

Table 3. Chemical composition of the analyzed powders provided in weight percent.

Powder	C	O	N	S	Si	Cr	Ni	Mn	Mo	P
316L VIGA	0.01	0.028	0.018	0.005	0.05	18.0	14.2	1.4	2.9	0.004
316L GA	0.013	0.066	0.14	0.007	0.7	16.5	12.3	1.5	2.5	0.02
316L WA	0.033	0.24	0.044	0.005	0.8	16.9	12.7	0.17	2.2	0.02

Attempts were also made to change the morphology of the WA powder through various mechanical methods to improve the powder properties.

5.1 LB-PBF process

In this work, two different EOS machines were used to produce specimens, an EOS M290 and an EOS M100, both located at Chalmers University of Technology. Both were equipped with an Nd:YAG laser source operating at a maximum power of 400W and 200W, respectively. The M100 has an effective laser spot size of approximately 50 µm in diameter, while the M290 has a laser spot size of 80 µm in diameter. Hence, the laser intensity of the M100 machine is almost double that of the M290. The atmosphere within the machines was purged using Ar gas with a 5.0 purity until an oxygen level of 0.1 % was reached. In the experiments, only bulk exposures with a layer rotation of 67° and a stripe length of 5 mm were used to build the samples.

5.2 Analysis Techniques

Light Optical Microscopy (LOM)

Throughout this work, a Zeiss Axio Imager M2M was used to capture polished and etched images for density determinations and microstructure characterizations. The microscope was equipped with an automatic stage, enabling cross-sections to be automatically switched. Images for density determinations were further analyzed using the imageJ software. Images were made binary through automatic thresholding operation, and pores/defects were measured with a built-in particle counter.

Scanning Electron Microscopy (SEM)

A scanning electron microscope is a very common tool for characterization within many scientific fields due to its high resolution, versatility, large depth of field and ease of use.

The imaging is produced through an interaction of the specimen with a focused electron beam accelerated to high voltages (up to 30 kV). The electrons are generated either through tungsten or LaB_6 filaments on the one hand or field-emission emitters on the other. The resulting resolution depends on the electron source, with the field emission gun (FEG) providing the brightest yet smallest beam, optimizing the resolution. The beam is focused and scanned over the surface of the sample through an array of magnetic lenses. As the electrons hit the surface of the sample, they interact with the electrons within the sample down to a depth of around 1–2 µm. However, the exact depth depends on the acceleration voltage, the density of the sample and the angle of the incident beam. The interaction is basically a scattering of the incoming electrons as they hit the sample surface that can be both inelastic and elastic. Elastic scattering (BSE) occurs when the incident electron interacts with the nucleus of the sample atom, bending its trajectory. Inelastic scattering occurs when the incident electron collides with the atom and transfers some of its energy to it. The two interactions are illustrated in Figure 11, which also shows the depths at which the interactions occur.

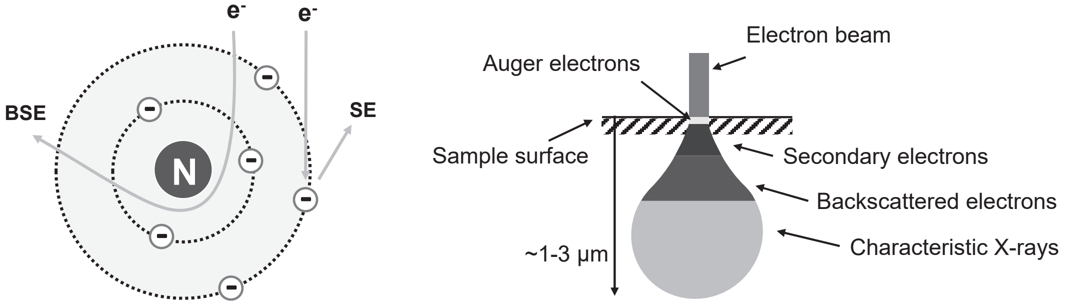

Figure 11. Schematics of incident electron interaction (left) and the interaction volume (right).

As the incident electron transfers its kinetic energy to the loosely bound outer-shell electrons, some escape from the atom as secondary electrons (SE). The emitted SE has a low kinetic energy, ~50 eV, and thus escapes from the surface of the sample. Secondary electrons provide topographic contrast for the sample surface and is the most commonly used imaging method. If, however, a greater amount of the energy is transferred to the inner-shell electrons, an inner-shell electron can be knocked off. This creates an electron hole that is filled by an outer shell electron, and this transition creates characteristic X-rays. These can be further used for chemical analysis in the SEM [60].

In this work, powder and etched microstructures were studied in a LEO Gemini 1550 FEG-SEM equipped with an X-Max EDX detector.

Transmission Electron Microscopy (TEM)

In transmission electron microscopy, an electron beam is accelerated to voltages between 100 kV and 300 kV and irradiates a thin sample. The electrons are generated and focused in a similar manner as in the SEM, with some instruments allowing similar scanning of the beam (STEM). As compared to SEM, in TEM, the wave characteristic of the electron is taken advantage of for the imaging, and as such, the resolution of the TEM can be much higher. As the beam passes through the sample, it interacts with it and forms an image. For the beam to be able pass through the sample, it must be electron transparent, and hence, samples must be very thin. The image is focused and magnified, then projected onto a fluorescent screen, which produces a viewable image. Contrast is generated through changes in the amplitude of the electron wave as it passes through the sample. Amplitude changes can occur due to variations in the thickness (or density) in the sample, creating a variation in the scattering. The diffraction contrast also influences the amplitude of the electrons. Depending on the crystal structure and its orientation, the electrons will be scattered differently and produce contrast changes.

Another feature of the TEM is the ability to analyze the crystal structure of specific constituents of a microstructure within a sample. As the electrons behave as a wave, when they pass through the sample the atoms in the sample act as a diffraction grating. Thus, a diffraction pattern forms and can be used to calculate lattice parameters [61].

In this work, two TEM microscopes were used: an FEI Titan operating at 300 kV and an FEI Tecnai T20 operating at 200 kV. Both were equipped with EDX systems and capable of running in STEM mode, which was utilized to analyze oxide particles in the LB-PBF built parts.

X-ray Diffraction (XRD)

X-ray diffraction (XRD) is a simple method of measuring the crystallographic structure of a material. By irradiating the sample with X-rays while simultaneously varying the angle of incidence, the inter-planar distances of a crystal can be determined according to the Bragg condition:

$$2dsin\theta = n\lambda \tag{8}$$

where d is the inter-planar distance between two crystallographic planes, θ is the angle at which the incident X-rays hits the sample, n is the diffraction order and λ the wavelength of the X-ray. At certain angles, the X-rays cause constructive interference, since the Bragg condition is fulfilled, which the detector is able to detect. At other angles, the interference is destructive, and the detector does not detect the X-rays [62]. Each crystalline arrangement has a number of well-defined angles in which the constructive interference occurs, making the identification of the crystalline structure of the sample possible by comparing the measured peaks to a database. XRD can also be used to give an indication of whether a sample has a preferential texture by comparing the amplitudes of the peaks relative to a powder reference. Since the powder will have a random orientation of grains, the relative amplitudes of individual peaks will be given by the number of reflections of a certain family of planes, for example, (110). If the sample strongly deviates from the powder reference, there is preferential a texture within the sample.

A Bruker AXD D8 Advance system equipped with a Cr X-ray source was used in this work, and the measurements were conducted using a Bragg–Brentano set-up. The source was operated at 35 kV and a current of 40 mA.

X-ray Photoelectron Spectroscopy (XPS)

X-ray photoelectron spectroscopy (XPS) is a surface-sensitive analytical method for chemical analysis with the ability to resolve chemical states within a sample, for example, if Fe is present as an oxide or as a metal. It probes up to 10 nm of the surface. X-ray photoelectron spectroscopy is not limited to certain elements, and thus, all elements except He and H can be successfully detected and quantified.

The working principle is that an X-ray beam irradiates a sample and the irradiation causes the atoms within the sample to ionize. During the process of ionization, the sample atom releases photoelectrons, which are detected by the XPS. The photoelectrons have a certain kinetic energy as they are emitted, and the energy is dependent on several factors, such as the element from which it is emitted, the specific electron orbital and the chemical bonding. The emitted photoelectrons are focused and analyzed in a hemispherical analyzer, which quantifies the kinetic energy of the electrons. The data is presented as the amount of counts as a function of the binding energy (BE). The BE relates to the initial kinetic energy according to the following equation:

$$E_B = hv - E_K - \Phi \tag{9}$$

where E_B is the BE, hv is the energy of the incident X-ray photon, E_K is the kinetic energy and Φ is the spectrometer work function of the system.

In this study, a PHI 5500 with a monochromatic Al K_α X-ray source was used to analyze the surface oxides of 316L powder. Survey spectra were collected using a 93 eV pass energy, with a 0.4 eV step. Narrow scans of elements of interest were collected at a 23.5 eV pass energy and a 0.1 eV step. The energy calibration of the system was performed using pure elemental standards of Ag, Au and Cu. The etch rate was calibrated using a Ta foil with electrochemically grown Ta_2O_5 with a defined thickness of 100 nm; therefore, all of the etch depths are related to the etch rate of Ta_2O_5.

Mechanical testing

Test coupons for impact and tensile testing were built according to the geometries, as described in the standards ISO 148-1 (Charpy V-notch) and ISO 2740, respectively. A set of specimens were heat-treated to alleviate stresses, which was done at 900 °C for 1 h in vacuum.

The impact toughness was tested using a 150 J anvil and performed according to the standard ISO 10045-1 using an Instron Wolpert pendulum tester. Similarly, tensile testing was performed according to the ISO 6892-1 standard using a Zwick Z100 tensile tester.

6. Summary of appended papers

This chapter aims to summarize the findings of the appended papers. All of the papers target the stainless-steel alloy 316L, which is a widely used alloy within LB-PBF processing. The first paper investigates the surface chemistry of the powder produced by different atomization techniques. The second paper investigates to what extent WA powder can be used within the LB-PBF process. The third paper conducts a detailed characterization of the oxides found within LB-PBF-processed parts.

6.1 Paper I - Effect of atomization on surface oxide composition in 316L stainless steel powders for additive manufacturing

The aim of the paper was to investigate how the surface chemistry changes as the atomization method changes from the industry standard vacuum inert gas atomized (VIGA) powder for a stainless steel 316L alloy.

Other than the VIGA powder, an air melted nitrogen gas atomized (GA) and a water-atomized (WA) powder were analyzed and compared. The initial SEM investigations, seen in Figure 12, showed that the VIGA powder contained few nanometric oxides, concentrated within the interdendritic areas of the powder surface. The appearance of the oxides was similar to splats. The GA powder had similar features, with the addition of larger hemispheres scattered throughout the surface. The WA powder had larger particulate features, with a flake-like morphology in addition to the features described for VIGA and GA. The flake-like particulates found on the WA powder seemed to have low cohesion to the surface. Based on the SEM observations of the powder surfaces, the VIGA powder was found to have the least amount of particulates, followed by the GA powder. The WA powder had the largest number of particulates decorating the powder surface.

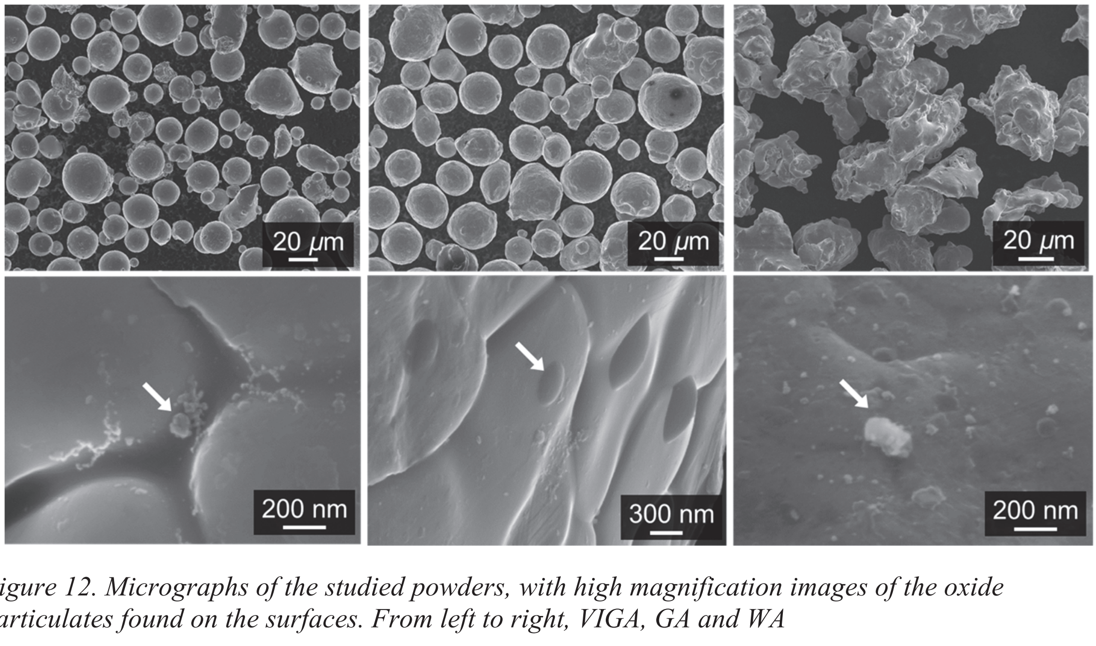

Figure 12. Micrographs of the studied powders, with high magnification images of the oxide particulates found on the surfaces. From left to right, VIGA, GA and WA

The XPS analysis revealed that Fe, Cr and Mn were preferentially present in the oxide state on surfaces of the VIGA and GA powders, and Si was also detected in the GA powder. The WA powder had primarily Si-based oxide on the surface, with smaller quantities of Cr and Fe.

Relative cation concentrations in the surface oxide as a function of the etch depth of the studied powder are presented in Figure 13. Combining the earlier SEM micrographs with the XPS depth profiling, it could be concluded that the elements with high oxygen affinity (Cr, Mn, Si) were enriched in the particulates imaged in Figure 12; however, significant Si contents were only found in the GA and WA powders. Additionally, surrounding the particulates was a thin Fe-rich oxide layer, whose thickness was calculated to be 4.1, 4.0 and 3.2 nm for the VIGA, GA and WA powders, respectively.

It was concluded that the differences between VIGA and GA powders were considered minimal, and hence, the use of GA powder within LB-PBF should not significantly affect the performance of components relative to a VIGA-produced component. The WA powder, by contrast, showed significant differences in the surface oxide state, the effects of which need to be further studied.

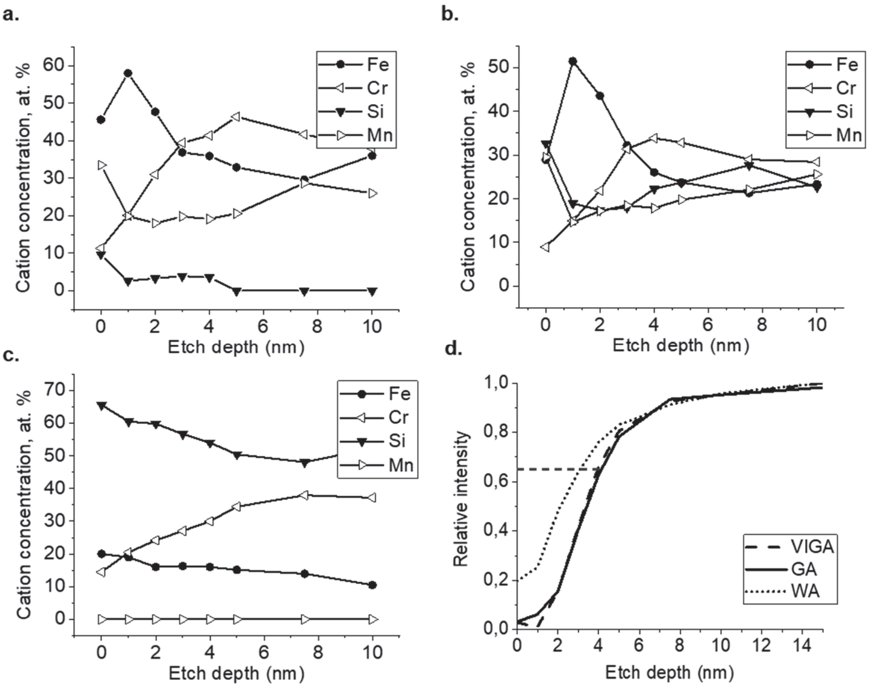

Figure 13. Calculated cation concentrations of oxides found on the surfaces of a) VIGA, b) GA and c) WA. d) Relative intensity of the Fe-metallic peak, allowing the thickness of the oxide layer to be calculated.

6.2 Paper II - Factors affecting printability of 316L powders using the DMLS process

This paper investigated the feasibility of using WA 316L powder within the LB-PBF process and whether secondary processing of the powder could improve its printability. The GA powder was included in the study as a reference. The powder properties were extensively studied using both conventional PM methods (see Table 4) and a powder rheometer. It was later concluded that while the powder rheometer provides large amounts of data, it also generates a large spread, and tests were found to be very time-consuming. Some of the data was also difficult to interpret, and it was difficult to determine whether it was relevant for the LB-PBF process.

Table 4. Physical properties of the tested powders and measured oxygen content of the powders after the modifications.

Powder	AD (g/cm^3)	TD (g/cm^3)	Flow (s/50g)	x_{10} (μm)	x_{50} (μm)	x_{90} (μm)	O (wt.%)
GA	4.3	4.9	18.1	26.1	42.2	63.3	0.07
WA	2.4	3.1	37.4	25.8	46.5	70.4	0.24
WA2	3.1	4.0	22.8	27.0	45.2	65.9	0.25
WA3	3.7	4.6	16.4	24.9	41.0	58.8	0.23

The results from the builds showed that when using a thin layer setting (20 μm) in an EOS M290 machine, the final build density was equal using WA powder compared to printing with the GA powder. Polished cross sections of the builds using a layer thickness of 20 μm are presented in Figure 14. No issues with spreadability of the WA powder were encountered, nor were any macro or micro defects detected. However, when printing using thicker layer settings (> 20 μm), the build density of the WA sample decreased relative to the GA sample, reaching a porosity of nearly 1%.

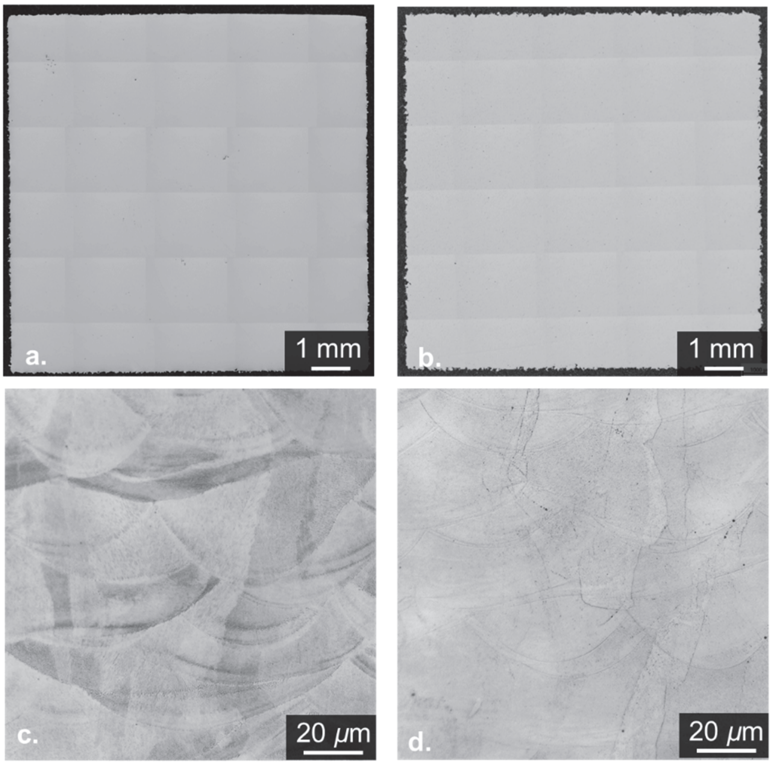

Figure 14. Polished X–Y cross sections of cubes built using a, b) 20 μm layer setting and c, d) etched cross sections. a, c) GA. b, d) WA.

Similar experiments were repeated in an M100 machine, including the WA powder, which had undergone secondary operations (WA2 and WA3). The results from these experiments can be viewed in Figure 15. A decrease in performance relative to the tests in the M290 machine was noted for the WA powder. However, higher final densities were reached using WA2 and WA3, as compared to the as-atomized counterpart (WA), although at a layer thicknesses of > 20 μm, the final build density was still low compared to the GA powder. Furthermore, the mechanical testing of samples printed using a layer thickness of 20 µm showed that the yield strength of the WA samples was around 100 MPa lower, compared to the GA samples; however both samples had similar elongation at fracture at 27% and 28%, respectively. The reason for the lower strength remained unclear.

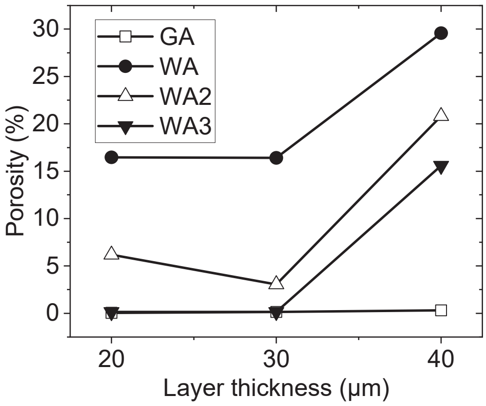

Figure 15. Porosity of built cubes in the EOS M100 machine as measured by LOM of the components produced using GA, WA, WA2 and WA3 powders.

Based on the observed results, the critical powder properties for LB-PBF processing appeared to be the apparent and tap densities. The observed performance decrease in the M100 was believed to be due to the higher intensity of the laser (the spot diameter is 40 µm in the M100), which over-heated the gas in the powder bed more easily. This caused disruptive melt pool instabilities, affecting the final density of the built samples. However, secondary operations on the WA powder were able to enhance performance without compromising its cost, making it into a viable powder alternative for LB-PBF. With that said, even with the secondary operations, there was an observed limit to the printability of the WA powder relative to the GA powder.

6.3 Paper III - Effect of the powder feedstock on the oxide dispersion strengthening of 316L stainless steel produced by laser powder bed fusion

This work investigated the concept of enhancing the precipitation response of oxides by using WA powder as a means of introducing a high volume fraction of fine oxide precipitates into the microstructure. The LB-PBF process, as indicated by previous studies [63]–[65], can promote a homogenous and fine precipitation of nanometric oxides. Therefore, it believed that the WA powder can provide an oxide dispersion strengthening effect, if the size and number density of oxide precipitates is optimized.

In this study, WA and GA (for reference) powders were used to build samples, from which thin-foils were prepared and further investigated using TEM. The micrographs from the investigation are shown below in Figure 16.

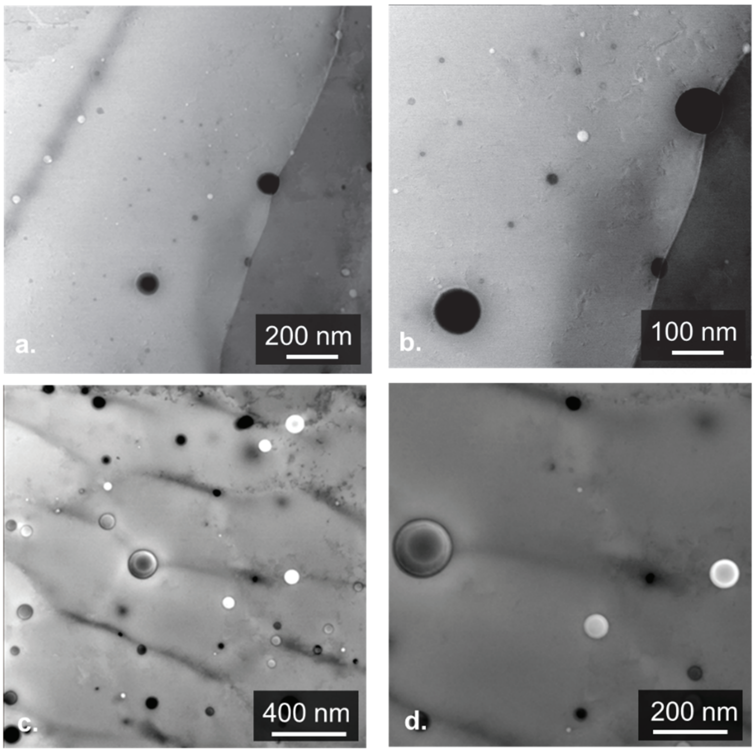

Figure 16. TEM micrographs from an a, b) GA sample and c, d) WA sample in the as-built condition.

The oxides were found to be spherical and homogeneously distributed within the microstructures of both samples. The average size of the oxides was 46 ± 25 and 56 ± 27 nm in the GA and WA samples, respectively. The size distribution can be found in Figure 17, and the counted number density of oxides was 1.6×10^7 and 1.3×10^7 mm^{-2} for the samples built from WA and GA powders, respectively. The difference between the two samples was found to be relatively minor, considering that the WA powder had around three times the amount of oxygen compared to the GA powder.

Additionally, the oxides were found to be amorphous in both samples. There also appeared to be two different oxide populations in both the GA and WA samples, one with a bright contrast and one with a dark contrast. These had consistent systematic compositional variations, with the dark oxides having contributions from the matrix elements, in addition to the oxide forming elements Cr and Si. Within the WA sample, numerous core-shell structures were observed, and the shell was found to be richer in Si relative to the core.

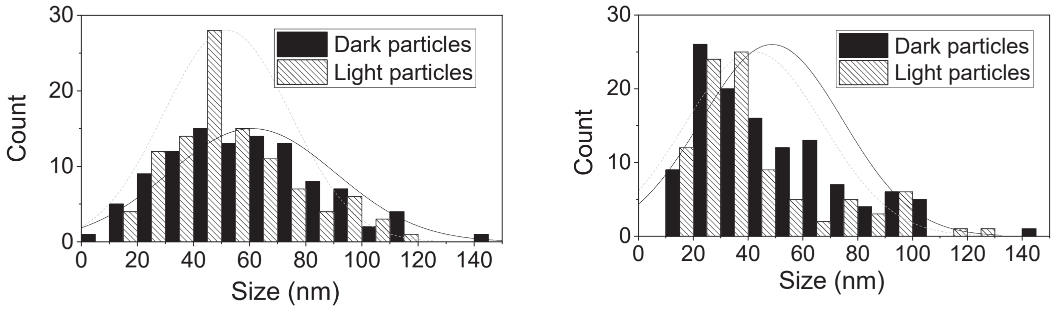

Figure 17. Summary of particle measurements in the as-built samples. Left: GA. Right: WA.

The chemical composition of the oxides found in the built specimens varied between the GA and WA samples; see Figure 18. Oxides enriched in Si with trace amounts of Mn and Al were found in the GA sample, while the WA sample contained oxides rich in Cr and lower amounts of Si. Relative to the findings in Paper I, the GA sample had undergone compositional changes of the oxides relative to the surface particulates, from Mn, Cr and Si particulates to a mainly Si-based oxide.

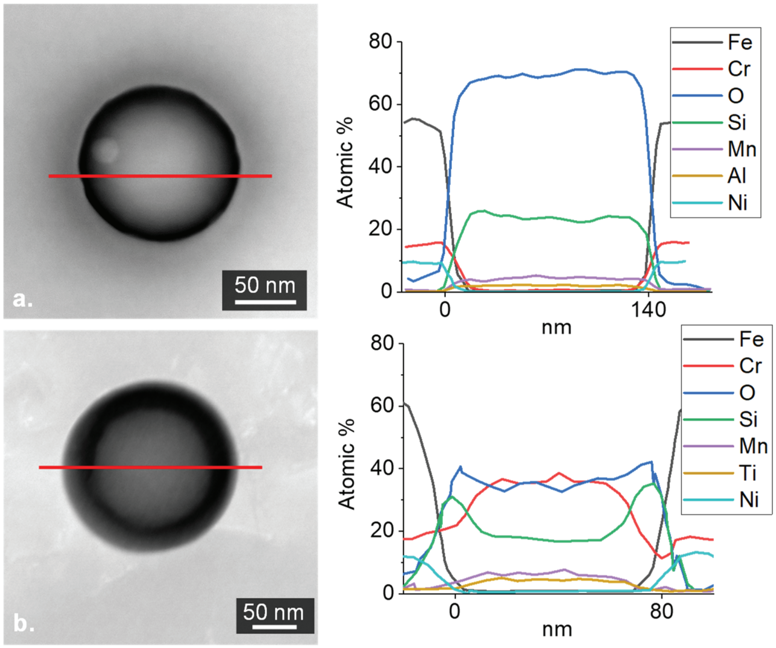

Figure 18. STEM HAADF images of oxides, with the corresponding EDX line scans. Top row: GA. Bottom row: WA.

Furthermore, it seems that oxides melt, disperse and, in the case of GA, reduce to mainly Si-oxide during LB-PBF processing. Taking into account that the large particulates found on the surfaces were rarely observed in the microstructures, this assumes the change in composition mentioned above and the morphological changes.

Even though it was possible to increase the number density of oxides using WA powder, no clear improvements in mechanical strength at room temperature were noted in comparison to the standard GA powder. However, the oxide size and the number density had not been optimized, and hence, further work is needed to achieve an ODS effect.

7. Conclusions

Based on the findings in this work, several conclusions can be drawn.

The stainless steel alloy 316L could be readily atomized using inert gases and water without any severe loss of alloying elements or extensive oxidation. Only minor differences in the oxide particulate coverage were observed between the VIGA and the GA powders, and the oxide particulates were found to be rich in Cr and Mn, with minor amounts of Si in the GA powder. The WA powder, however, had significantly higher oxide particulate coverage and was found to contain mainly Si and Cr. The Fe-rich oxide layer covering the remainder of the powder surface, was found to be around 4 nm for the VIGA and GA powders and around 3 nm for the WA powder.

The WA powder was able to be spread and printed to full density using a 20 µm layer in the LB-PBF process. However, using a layer thickness of 40 µm resulted in ~1% porosity, whereas the GA powder displayed ~0.06% porosity. These issues were found not to be due to the surface oxide characteristics or the overall higher oxygen content. Rather, the morphology of the WA powder caused the low powder bed densities that created melt pool instabilities, hence resulting in the high porosity of the component. Additionally, it was found that the WA powder could with ease be modified for improved printability and should be considered for future AM use as a low-cost alternative to VIGA powder.

A fine and homogenous oxide precipitation was found after the LB-PBF processing of both the GA and WA powders. Furthermore, it was possible to affect the in-situ oxide precipitation by using the WA powder. The number density of oxides increased from 1.3×10^7 in the GA sample to 1.6×10^7 mm^{-2} in the WA sample. The average oxide size was found to be 46 ± 25 and 56 ± 27 nm in the GA and WA samples, respectively. It was also found that the oxides in the GA sample mainly contained Si, while the oxides in the WA sample contained Cr and Si. The oxides were found to undergo a chemical and morphological transformation relative to oxide particulates found on the surfaces, hence it is believed that oxides melt and disperse during processing. During mechanical testing at ambient temperature and at 550°C, no strengthening effect was noted for the WA sample; by contrast, the yield strength decreases by ~100 MPa at room temperature and ~30 MPa at 550°C, compared to the GA sample.

8. Future work

Based on the findings and conclusions of this work, the following is suggested for future research.

Since no obvious defects in the LB-PBF processed parts were observed as the atomizing media was varied, it could be of interest to explore other variations in alloying of the alloy 316L. One example is removing Si from the air-melted grades to see whether the powder surface oxide products start influencing the build quality. Another is to explore other alloys as an attempt to define which elements are detrimental to LB-PBF processing, and in which quantities.

By further investigating the oxide precipitation response, it would be possible to understand the mechanism behind the large scatter in the number density of oxides within the WA sample. Thus, number densities of up to five times greater could be achieved. Attempts to tailor the precipitation response through parameter variation during LB-PBF processing can also be explored, as previous research and modeling efforts suggest that it is viable. Another method of altering the oxide precipitation could be through micro alloying, using elements with high affinity to oxygen yet sluggish diffusion and promoting homogenous nucleation but limiting growth.

While no strengthening effect was directly observed from the oxide precipitates at the studied number density, their effect on the long-term microstructural stability is worth considering. It is likely that they can have a Zener pinning effect, preventing grain coarsening during high-temperature heat treatments. The 900 °C treatment did cause the cells to dissolve, but no re-crystallization had occurred. The particle-dislocation interaction is also worth looking further into to definitively conclude whether the oxides have positive contributions to the performance of the material.

9. Acknowledgements

First, I would like to thank Höganäs AB, especially Sigurd Berg, for believing in me and giving me the opportunity to conduct this work.

I would also like to thank my supervisors, Adj. Prof. Sven Bengtsson and Prof. Eduard Hryha, for their endless support, guidance and help throughout this time.

A special thanks goes to Dr. Masoud Rashidi, who inspired me and supported me in many aspects of this work. Without his support, much of the results in this thesis would not have been possible.

Furthermore, I would like to acknowledge the following people for their help regarding practical aspects: Roger Sagdahl, Håkan Millqvist and Dr. Yiming Yao. Additionally, I would like to thank Dr. Eric Tam for all the support and help with maintaining the old XPS.

I would also like to acknowledge all my colleagues at Höganäs for their help, fruitful discussions and laughs. And of course, this extends to all my colleagues at Chalmers, who understand the trying times of this journey and provide support and joy when it is needed the most.

Finally, none of this would have been possible if not for all of my amazing, kind, funny and supportive friends and family. Thanks for sticking around through both vått och torrt.

10. References

[1] D. S. Thomas and S. W. Gilbert, "Costs and Cost Effectiveness of Additive Manufacturing," Dec. 2014, Accessed: Mar. 04, 2020. [Online]. Available: https://www.nist.gov/publications/costs-and-cost-effectiveness-additive-manufacturing.

[2] International Organization for Standardization, "17296-2 - Additive Manufacturing—General Principles—Part2: Overview of Process Categories and Feedstock," Geneva, Switzerland, ISO Standard No. 17296-2, 2016.

[3] "EOS Metal Materials for Additive Manufacturing," 2020. https://www.eos.info/material-m (accessed Feb. 04, 2020).

[4] "EBM-Built Materials - Arcam AB," 2020. http://www.arcam.com/technology/electron-beam-melting/materials/ (accessed Feb. 04, 2020).

[5] "Metal 3D Printing Materials - Optomec Additive Manufacturing," *Optomec*, 2018. https://optomec.com/3d-printed-metals/lens-materials/ (accessed Feb. 04, 2020).

[6] "Metal 3D Printing Materials & Binders," 2020. https://www.exone.com/en-US/3d-printing-materials-and-binders/metal (accessed Feb. 04, 2020).

[7] "Materials - Digital Metal," 2020. https://digitalmetal.tech/materials/ (accessed Feb. 04, 2020).

[8] "Office friendly metal 3D printing | Desktop Metal." https://www.desktopmetal.com/products/materials/studio-system/ (accessed Feb. 04, 2020).

[9] A. Vance, "3-D Printing is Spurring a Manufacturing Revolution," *The New York Times*, Sep. 13, 2010.

[10] G. Li *et al.*, "In vitro and in vivo study of additive manufactured porous Ti6Al4V scaffolds for repairing bone defects," *Scientific Reports*, vol. 6, no. 1, p. 34072, Dec. 2016, doi: 10.1038/srep34072.

[11] T. Tampi, *Smartech report: 3D printing in dental market to reach $3.1 billion by 2020*. 2015.

[12] M. Cotteleer and J. Crane, "3D Opportunity in Tooling," 2014. Accessed: Jan. 09, 2020. [Online]. Available: https://www2.deloitte.com/us/en/insights/focus/3d-opportunity/additive-manufacturing-3d-opportunity-in-tooling.html.

[13] C. Körner, "Additive manufacturing of metallic components by selective electron beam melting — a review," *International Materials Reviews*, vol. 61, no. 5, pp. 361–377, Jul. 2016, doi: 10.1080/09506608.2016.1176289.

[14] J. Milberg and M. Sigl, "Electron beam sintering of metal powder," *Production Engineering*, vol. 2, no. 2, pp. 117–122, 2008.

[15] W. E. Frazier, “Metal Additive Manufacturing: A Review,” *Journal of Materials Engineering and Performance*, vol. 23, no. 6, pp. 1917–1928, Jun. 2014, doi: 10.1007/s11665-014-0958-z.

[16] M. Thomas, G. J. Baxter, and I. Todd, “Normalised model-based processing diagrams for additive layer manufacture of engineering alloys,” *Acta Materialia*, vol. 108, pp. 26–35, Apr. 2016, doi: 10.1016/j.actamat.2016.02.025.

[17] J. C. Ion, H. R. Shercliff, and M. F. Ashby, “Diagrams for laser materials processing,” *Acta Metallurgica et Materialia*, vol. 40, no. 7, pp. 1539–1551, Jul. 1992, doi: 10.1016/0956-7151(92)90097-X.

[18] A. Strondl, O. Lyckfeldt, H. Brodin, and U. Ackelid, “Characterization and Control of Powder Properties for Additive Manufacturing,” *JOM*, vol. 67, no. 3, pp. 549–554, Mar. 2015, doi: 10.1007/s11837-015-1304-0.

[19] A. B. Spierings, M. Voegtlin, T. Bauer, and K. Wegener, “Powder flowability characterisation methodology for powder-bed-based metal additive manufacturing,” *Progress in Additive Manufacturing*, vol. 1, no. 1–2, pp. 9–20, 2016.

[20] Y. Sun, S. Gulizia, C. Oh, C. Doblin, Y. Yang, and M. Qian, “Manipulation and characterization of a novel titanium powder precursor for additive manufacturing applications,” *JOM*, vol. 67, no. 3, pp. 564–572, 2015.

[21] J. Clayton, “Characterising powders to optimise additive manufacturing,” *TCT Magazine*, Jun. 06, 2014. https://www.tctmagazine.com/api/content/a800c0da-ed7f-11e3-bf54-22000a4f82a6/ (accessed Jan. 13, 2020).

[22] S. Vock, B. Klöden, A. Kirchner, T. Weißgärber, and B. Kieback, “Powders for powder bed fusion: a review,” *Progress in Additive Manufacturing*, vol. 4, no. 4, pp. 383–397, Dec. 2019, doi: 10.1007/s40964-019-00078-6.

[23] P. Karapatis, “A sub-process approach of selective laser sintering,” 2005, doi: 10.5075/EPFL-THESIS-2506.

[24] E. H. Amara and R. Fabbro, “Modelling of gas jet effect on the melt pool movements during deep penetration laser welding,” *J. Phys. D: Appl. Phys.*, vol. 41, no. 5, p. 055503, Feb. 2008, doi: 10.1088/0022-3727/41/5/055503.

[25] T. Debroy and S. A. David, “Physical processes in fusion welding,” *Reviews of Modern Physics*, vol. 67, no. 1, pp. 85–112, 1995, doi: 10.1103/RevModPhys.67.85.

[26] K. C. Mills, B. J. Keene, R. F. Brooks, and A. Shirali, “Marangoni effects in welding,” *Philosophical Transactions of the Royal Society of London A: Mathematical, Physical and Engineering Sciences*, vol. 356, no. 1739, pp. 911–925, Apr. 1998, doi: 10.1098/rsta.1998.0196.

[27] U. Scipioni Bertoli, G. Guss, S. Wu, M. J. Matthews, and J. M. Schoenung, “In-situ characterization of laser-powder interaction and cooling rates through high-speed imaging of powder bed fusion additive manufacturing,” *Materials & Design*, vol. 135, pp. 385–396, Dec. 2017, doi: 10.1016/j.matdes.2017.09.044.

[28] D. Bergström, J. Powell, and A. F. H. Kaplan, “The absorptance of steels to Nd:YLF and Nd:YAG laser light at room temperature,” *Applied Surface Science*, vol. 253, no. 11, pp. 5017–5028, 2007, doi: https://doi.org/10.1016/j.apsusc.2006.11.018.

[29] A. Simchi, “Direct laser sintering of metal powders: Mechanism, kinetics and microstructural features,” *Materials Science and Engineering: A*, vol. 428, no. 1, pp. 148–158, 2006, doi: https://doi.org/10.1016/j.msea.2006.04.117.

[30] P. Bidare, I. Bitharas, R. M. Ward, M. M. Attallah, and A. J. Moore, “Fluid and particle dynamics in laser powder bed fusion,” *Acta Materialia*, vol. 142, pp. 107–120, Jan. 2018, doi: 10.1016/j.actamat.2017.09.051.

[31] S. A. Khairallah, A. T. Anderson, A. Rubenchik, and W. E. King, “Laser powder-bed fusion additive manufacturing: Physics of complex melt flow and formation mechanisms of pores, spatter, and denudation zones,” *Acta Materialia*, vol. 108, pp. 36–45, Apr. 2016, doi: 10.1016/j.actamat.2016.02.014.

[32] S. Ly, A. M. Rubenchik, S. A. Khairallah, G. Guss, and M. J. Matthews, “Metal vapor micro-jet controls material redistribution in laser powder bed fusion additive manufacturing,” *Scientific Reports*, vol. 7, no. 1, p. 4085, Jun. 2017, doi: 10.1038/s41598-017-04237-z.

[33] C. L. A. Leung, S. Marussi, R. C. Atwood, M. Towrie, P. J. Withers, and P. D. Lee, “In situ X-ray imaging of defect and molten pool dynamics in laser additive manufacturing,” *Nat Commun*, vol. 9, no. 1, pp. 1–9, Apr. 2018, doi: 10.1038/s41467-018-03734-7.

[34] I. Campbell, O. Diegel, J. Kowen, and T. Wohlers, *Wohlers report 2018: 3D printing and additive manufacturing state of the industry: annual worldwide progress report*. Wohlers Associates, 2018.

[35] C. Choudhury and H. Kemmer, *Vacuum Melting and Remelting Processes*, Casting., vol. 15. ASM International, 1988.

[36] C. T. Sims, N. S. Stoloff, and W. C. Hagel, *Superalloys II*, 2nd ed. Wiley, 1987.

[37] W. M. Haynes, *CRC Handbook of Chemistry and Physics, 92nd Edition*. Taylor & Francis, 2011.

[38] C. F. Dixon, “Atomizing molten metals — a review,” *Canadian Metallurgical Quarterly*, vol. 12, no. 3, pp. 309–322, Jul. 1973, doi: 10.1179/cmq.1973.12.3.309.

[39] I. E. Anderson, E. M. H. White, and R. Dehoff, “Feedstock powder processing research needs for additive manufacturing development,” *Current Opinion in Solid State and Materials Science*, vol. 22, no. 1, pp. 8–15, Feb. 2018, doi: 10.1016/j.cossms.2018.01.002.

[40] A. Ünal, “Influence of nozzle geometry in gas atomisation of rapidly solidified aluminium alloys,” *Materials Science and Technology*, vol. 4, no. 10, pp. 909–915, Oct. 1988, doi: 10.1179/mst.1988.4.10.909.

[41] R. Ünal, “Improvements to close coupled gas atomisation nozzle for fine powder production,” *Powder Metallurgy*, vol. 50, no. 1, pp. 66–71, Mar. 2007, doi: 10.1179/174329007X164899.

[42] A. Ünal, "Effect of processing variables on particle size in gas atomization of rapidly solidified aluminium powders," *Materials Science and Technology*, vol. 3, no. 12, pp. 1029–1039, Dec. 1987, doi: 10.1179/mst.1987.3.12.1029.

[43] I. Olefjord and L. Nyborg, "Surface Analysis of Gas Atomized Ferritic Steel Powder," *Powder Metallurgy*, vol. 28, no. 4, pp. 237–243, Jan. 1985, doi: 10.1179/pom.1985.28.4.237.

[44] B. H. Rabin, G. R. Smolik, and G. E. Korth, "Characterization of entrapped gases in rapidly solidified powders," *Materials Science and Engineering: A*, vol. 124, no. 1, pp. 1–7, Apr. 1990, doi: 10.1016/0921-5093(90)90328-Z.

[45] F. Persson, A. Eliasson, and P. Jönsson, "Prediction of particle size for water atomised metal powders: parameter study," *Powder Metallurgy*, vol. 55, no. 1, pp. 45–53, Feb. 2012, doi: 10.1179/1743290111Y.0000000016.

[46] Y. Seki, S. Okamoto, H. Takigawa, and N. Kawai, "Effect of atomization variables on powder characteristics in the high-pressured water atomization process," *Metal Powder Report*, vol. 45, no. 1, pp. 38–40, Jan. 1990, doi: 10.1016/S0026-0657(10)80014-1.

[47] T. Takeda *et al.*, "Method and apparatus for production of metal powder by atomizing," US6254661B1, Jul. 03, 2001.

[48] I. Olefjord and A. Nylund, "Surface reactions during rapid solidification and handling of Al5Mn2.5Cr powders," *Surface and Interface Analysis*, vol. 12, no. 7, pp. 401–406, 1988, doi: 10.1002/sia.740120707.

[49] M. Norell, L. Nyborg, and I. Olefjord, "Reactions during atomization of martensitic stainless steel," *Advances in Powder Metallurgy*, vol. 1, pp. 41–54, 1992.

[50] L. Nyborg, M. Norell, and I. Olefjord, "Surface studies of powder metallurgical stainless steel," *Surface and Interface Analysis*, vol. 19, no. 1–12, pp. 607–614, 1992, doi: 10.1002/sia.7401901113.

[51] I. Nyborg, T. Tunberg, and P. X. Wang, "Surface product formation during water atomization and sintering of austenitic stainless steel powder," *Metal Powder Report*, vol. 45, no. 11, pp. 750–753, Nov. 1990, doi: 10.1016/0026-0657(90)90459-T.

[52] T. Tunberg and L. Nyborg, "Surface Reactions During Water Atomisation and Sintering of Austenitic Stainless Steel Powder," *Powder Metallurgy*, vol. 38, no. 2, pp. 120–130, Jan. 1995, doi: 10.1179/pom.1995.38.2.120.

[53] E. Hryha, C. Gierl, L. Nyborg, H. Danninger, and E. Dudrova, "Surface composition of the steel powders pre-alloyed with manganese," *Applied Surface Science*, vol. 256, no. 12, pp. 3946–3961, Apr. 2010, doi: 10.1016/j.apsusc.2010.01.055.

[54] G. A. Rao, M. Srinivas, and D. S. Sarma, "Effect of oxygen content of powder on microstructure and mechanical properties of hot isostatically pressed superalloy Inconel 718," *Materials Science and Engineering: A*, vol. 435, pp. 84–99, 2006, doi: 10.1016/j.msea.2006.07.053.

[55] S. S. Babu, S. A. David, J. M. Vitek, and K. Mundra, "Model for inclusion formation in low alloy steel welds," *Science and Technology of Welding and Joining*, vol. 4, no. 5, pp. 276–284, Oct. 1999, doi: 10.1179/136217199101537879.

[56] S. S. Babu, S. A. David, and T. DebRoy, "Coarsening of oxide inclusions in low alloy steel welds," *Science and Technology of Welding and Joining*, vol. 1, no. 1, pp. 17–27, Feb. 1996, doi: 10.1179/stw.1996.1.1.17.

[57] S. S. Babu, F. Reidenbach, S. A. David, T. Böllinghaus, and H. Hoffmeister, "Effect of high energy density welding processes on inclusion and microstructure formation in steel welds," *Science and Technology of Welding and Joining*, vol. 4, no. 2, pp. 63–73, Apr. 1999, doi: 10.1179/136217199101537581.

[58] T. Matsumiya, T. Koseki, W. Yamada, and Y. Ueshima, "Mathematical analysis of segregation and compositional changes of nonmetallic inclusions in steel during solidification," *Nippon Steel Technical Report(Japan)*, vol. 57, pp. 50–56, 1993.

[59] H. Gruber, C. Luchian, E. Hryha, and L. Nyborg, "Effect of Powder Recycling on Defect Formation in Electron Beam Melted Alloy 718," *Metall and Mat Trans A*, vol. 51, no. 5, pp. 2430–2443, May 2020, doi: 10.1007/s11661-020-05674-8.

[60] J. Goldstein *et al.*, *Scanning Electron Microscopy and X-Ray Microanalysis: A Text for Biologists, Materials Scientists, and Geologists*. Springer US, 1981.

[61] C. B. Carter and D. B. Williams, *Transmission electron microscopy: Diffraction, imaging, and spectrometry*. Springer, 2016.

[62] W. H. Bragg and W. L. Bragg, "The reflection of X-rays by crystals," *Proceedings of the Royal Society of London. Series A, Containing Papers of a Mathematical and Physical Character*, vol. 88, no. 605, pp. 428–438, Jul. 1913, doi: 10.1098/rspa.1913.0040.

[63] K. Saeidi, L. Kvetková, F. Lofaj, and Z. Shen, "Austenitic stainless steel strengthened by the in situ formation of oxide nanoinclusions," *RSC Adv.*, vol. 5, no. 27, pp. 20747–20750, Feb. 2015, doi: 10.1039/C4RA16721J.

[64] Y. M. Wang *et al.*, "Additively manufactured hierarchical stainless steels with high strength and ductility," *Nature Materials*, vol. 17, no. 1, pp. 63–71, Oct. 2017, doi: 10.1038/nmat5021.

[65] F. Yan, W. Xiong, E. Faierson, and G. B. Olson, "Characterization of nano-scale oxides in austenitic stainless steel processed by powder bed fusion," *Scripta Materialia*, vol. 155, pp. 104–108, Oct. 2018, doi: 10.1016/j.scriptamat.2018.06.011.